

Supplementary Information: Side-impact collisions of Ar with NO

Cornelia G. Heid, Victoria Walpole, Mark Brouard, Pablo G. Jambrina, and F.
Javier Aoiz

Contents

1	Method details	2
1.1	Bond-axis orientation <i>versus</i> alignment	2
1.2	Theory	3
1.2.1	Bond-axis orientation in an arbitrarily oriented electric field	3
1.3	Data analysis	10
1.3.1	Experimental images	10
1.3.2	Conversion from the time-of-flight frame to the scattering frame	11
1.3.3	Simulation and fitting of the experimental images	13
2	The origin of the structure in the x-axis oriented DCSs	15
2.1	DCSs for x - and z -axis orientation at infinite field	15
2.2	Orientation dependent rotational rainbow structure	18
2.3	Quantum interference effect on intensities	21
2.4	Dependence on the static field	23

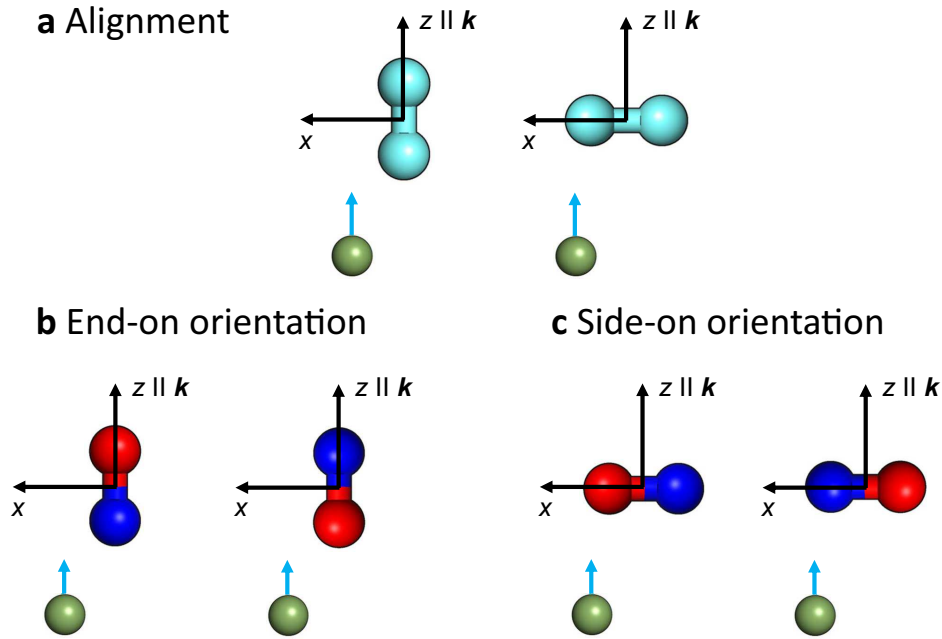
1 Method details

1.1 Bond-axis orientation *versus* alignment

It is important to recognise that there is a distinction to be made between orientation and alignment of molecules in space [1]. Since in the current study we are dealing with the spatial distribution of the NO bond axis, we will use the NO molecule to illustrate this difference. The concepts are general and applicable to any kind of open-shell or symmetric top molecule with some sort of directional anisotropy, such as a principal rotation axis or a permanent dipole moment.

Alignment of the internuclear bond axis, \mathbf{r} , refers to a spatial distribution that is either parallel or perpendicular to an axis of reference (“end *versus* side”), as depicted in Supplementary Fig. 1a. *Orientation* on the other hand, refers to a spatial distribution that is either parallel or antiparallel to the reference axis (Supplementary Fig. 1b and c). Hence, orientation can be along (“head *versus* tail”, $\pm z$ -orientation, Supplementary Fig. 1b), or perpendicular to the molecular axis (one side *versus* the other, $\pm x$ orientation, Supplementary Fig. 1c). In the latter case, when the molecule is *oriented*, we can distinguish between collisions at either end or either side. If a molecule is *aligned*, we can distinguish between collisions hitting the end or the side of the molecule, but no information is available about which end or which side the atom impacts on. Mathematically, the spatial distribution of the bond axis can be quantified by a set of polarisation moments, which, in turn, can be of odd or even rank, with odd moments describing orientation and even moments alignment. For molecules in a well defined rotational state, j , the maximum rank that can be used to describe their spatial configuration is $k_{\max} = 2j$ [1]. For the NO molecules in our experiment, which are state-selected in their ground electronic and rotational state with $j = 1/2$, then $k_{\max} = 1$. The molecules can therefore only be oriented, but not aligned.

It should be emphasised that we are dealing here with internuclear axis, \mathbf{r} , orientation as opposed to rotational angular momentum, \mathbf{j} , orientation [2]. The former is achieved by means of an external orienting field *via* the Stark effect. For sharp, well defined j states, the molecule must be either open shell or symmetric top for axis orientation. In contrast, rotational angular momentum orientation, which can be accomplished using circularly polarised light, does not produce molecu-



Supplementary Figure 1: Illustration of the difference between (a) *alignment* and (b) *end-on orientation*, and (c) *side-on orientation* of the internuclear axis (\mathbf{r}) of NO in the scattering frame (z -axis parallel to \mathbf{k}). In panel a, the molecule is *aligned* either along the z - or the x -axis, with equal probabilities for either end to be pointing up or down, and left or right, leading to head-on and side-on encounters, respectively. The molecule is *oriented* when the internuclear axis points in a specific direction along the axis of reference. In the examples shown in panels (b) and (c), the NO is oriented either parallel or antiparallel to the z -axis or the x -axis, respectively, in the latter case as in the current experiment.

lar axis orientation. We also note that in the experiments described in the present work, the bond axis is not strictly oriented (in the classical sense) along the field direction, \mathbf{E} , but is distributed according to the relatively broad probability distribution shown in the inset panel to Fig. 1a of the main text [3], where we compare the isotropic (no field) distribution, in grey, with the experimental distribution (red).

1.2 Theory

1.2.1 Bond-axis orientation in an arbitrarily oriented electric field

The newly developed quantum mechanical (QM) treatment used here to model the collisions of Ar atoms with NO molecules is valid for any arbitrary orientation of the electric field and may be applied to a range of collision systems. It will be shown that the z -orientation (when \mathbf{E} is parallel

or antiparallel to \mathbf{k}) is accounted for by a particular case of the general equation, in which some terms go to zero and the derivations of the relevant expressions are simplified [3–5]. Similarly, collisions taking place when the field is along the x -axis of the scattering frame constitute a particular case of the general expression with a clear dependence on specific terms. It will also be shown that the measurement of the resulting DCSs for these two orientations leads to the determination of the r -polarisation dependent differential cross sections [6] (r -PDDCSs) that provide the maximum possible information regarding the \mathbf{k} - \mathbf{r} - \mathbf{k}' vector correlation, where \mathbf{k}' is the product recoil velocity, and allow one to calculate the effect of any possible orientation on the DCS.

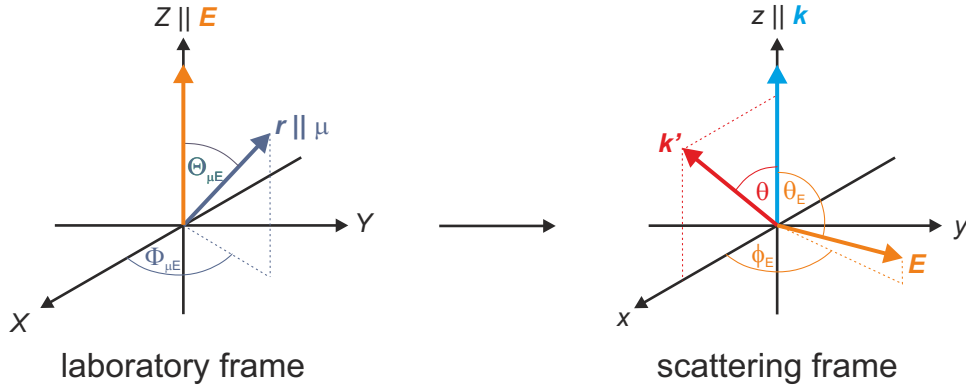
We define the static field direction with respect to the scattering frame (whose z -axis lies along the initial relative velocity, \mathbf{k} , and the xz hemi-plane contains the initial and final velocities, \mathbf{k} and \mathbf{k}' ; see Fig. 1a of the main text). In this work we have examined in detail side-on collisions, in which the orienting electric field (and hence, preferentially, the NO internuclear axis) is oriented along the x -axis in the scattering frame. In this sense, the theory is an extension of the previous theoretical treatment of the end-on (z -axis) orientation configuration, in which the direction of the orienting field is along \mathbf{k} [3–5].

The NO molecules in the present experiments are state-selected in the low-field seeking Λ -doublet state of the lowest rotational state, that is, $|j m \Omega \epsilon\rangle = |\frac{1}{2} \pm \frac{1}{2} \frac{1}{2} f\rangle$, where j is the rotational state, m is the projection of \mathbf{j} onto the relative velocity vector, \mathbf{k} , and Ω is the absolute value of the quantum number for the projection of \mathbf{j} onto the molecular bond axis, \mathbf{r} . The symmetry index, ϵ , which is related to the parity by $p = \epsilon(-1)^{j-1/2}$, can be either -1 (f) or $+1$ (e).

The state-to-state differential cross section (DCS) in the absence of a static electric field, and when both initial and final states are completely defined, is:

$$d\sigma(jm\Omega\epsilon \rightarrow j'm'\Omega'\epsilon') = \frac{1}{k^2} \left| f_{j'm'\Omega'\epsilon', jm\Omega\epsilon}(\theta) \right|^2, \quad (1)$$

where $f_{j'm'\Omega'\epsilon', jm\Omega\epsilon}(\theta)$ is the scattering amplitude whose explicit expression may be found elsewhere [4, 7]. When the orbital angular momentum representation is used in the scattering expressions, m and m' refer to the projections of \mathbf{j} and \mathbf{j}' along the initial relative velocity, \mathbf{k} .



Supplementary Figure 2: Relationship between the laboratory and the scattering frame. In the laboratory frame, the Z -axis is defined by the direction of the electric field, \mathbf{E} , while in the scattering frame, the z -axis is given by the relative velocity vector, \mathbf{k} , and the xz -plane is defined by \mathbf{k} and \mathbf{k}' , with θ denoting the scattering angle. The direction of the dipole moment, $\boldsymbol{\mu}$, which is parallel to the direction of the internuclear bond axis, \mathbf{r} , is given by the angles $\Theta_{\mu E}$ and $\Phi_{\mu E}$. The angles θ_E and ϕ_E describe the direction of the electric field in the scattering frame. In the present experiments the $+x$ orientation corresponds to $\theta_E = \pi/2$ and $\phi_E = 0$ (corresponding to a preference for repulsive side-on scattering towards the N-side of NO), and the $-x$ orientation to $\theta_E = \pi/2$ and $\phi_E = \pi$ (corresponding to a preference for repulsive side-on scattering towards the O-side of NO).

Hereinafter we will simplify the notation and write for given j and j' , Ω and Ω' values:

$$f_{j'm'\Omega'\epsilon',jm\Omega\epsilon}(\theta) \equiv F_{m'\epsilon'm\epsilon}. \quad (2)$$

Summing over m' and averaging over initial m we obtain the DCS for the $|j \Omega \epsilon\rangle \rightarrow |j' \Omega' \epsilon'\rangle$ transition:

$$d\sigma(j \Omega \epsilon \rightarrow j' \Omega' \epsilon') = \frac{1}{k^2(2j+1)} \sum_m \sum_{m'} |F_{m'\epsilon'm\epsilon}|^2. \quad (3)$$

We now need to consider two reference frames (see Supplementary Fig. 2). The first one, the laboratory frame, is defined by the direction of the static orienting field, \mathbf{E} . The preparation of internuclear axes is referenced to this frame, in which the direction of the internuclear axis, \mathbf{r} (which is taken $\uparrow\uparrow \boldsymbol{\mu}$, the dipole moment), is defined by the angle between \mathbf{r} and \mathbf{E} , denoted by $\Theta_{\mu E}$. Note that the direction of \mathbf{r} is defined from the N-end to the O-end of the molecule and that of \mathbf{E} from $+$ \rightarrow $-$ (see Fig. 1 of the main text). The second frame is the scattering frame, whose z -axis is along the initial relative velocity, \mathbf{k} , and where $\mathbf{k} - \mathbf{k}'$ defines the xz -plane. The direction of \mathbf{E} in this frame is given by the polar and azimuthal angles θ_E and ϕ_E , respectively.

Upon interaction with the electric field, the initially selected state evolves into a superposition

of the field-free e and f Λ -doublet states [4, 7–9],

$$\begin{aligned} |jm_E \Omega \hat{\mathbf{E}}\rangle &= \frac{1}{\sqrt{2}} \left[\alpha |jm_E \Omega e\rangle + \beta |jm_E \Omega f\rangle \right] \\ &= \frac{1}{2} \left[(\alpha + \beta) |jm_E \Omega\rangle + (\alpha - \beta) |jm_E - \Omega\rangle \right]. \end{aligned} \quad (4)$$

where m_E is the projection of \mathbf{j} onto the orienting electric field and α and β are the field-dependent mixing parameters,

$$|\alpha(E)| = \sqrt{1 - \frac{1}{\sqrt{1 + E_{\text{red}}^2}}}, \quad |\beta(E)| = \sqrt{1 + \frac{1}{\sqrt{1 + E_{\text{red}}^2}}}, \quad (5)$$

with the reduced field, E_{red} , given by the relative strength of the orienting Stark field, W_{Stark} , and the Λ -doublet splitting, E_Λ :

$$E_{\text{red}} = \frac{2W_{\text{Stark}}}{E_\Lambda}. \quad (6)$$

In the limit of $|\mathbf{E}| \rightarrow \infty$, $\alpha = \pm\beta = 1$, and hence the maximally oriented states $|jm_E + \Omega \hat{\mathbf{E}}\rangle$ and $|jm_E - \Omega \hat{\mathbf{E}}\rangle$ are produced. As noted in the main text, at the static electric fields employed, the Λ -doublet levels of the excited NO rotational states populated after collision are not significantly mixed, due to the rapid increase in Λ -doublet splitting with j' and the decrease in the Stark splitting.

The scattering amplitude for the $|jm_E \Omega \hat{\mathbf{E}}\rangle \rightarrow |j'm' \Omega' \epsilon'\rangle$ transition can be written as

$$F_{m'\epsilon' m_E \hat{\mathbf{E}}} = \frac{1}{\sqrt{2}} \sum_m D_{m m_E}^j(\phi_E, \theta_E, 0) [\alpha F_{m'\epsilon' m e} + \beta F_{m'\epsilon' m f}]. \quad (7)$$

In the present work $j = \Omega = \Omega' = \frac{1}{2}$. The $D_{m, m_E}^j(\phi_E, \theta_E, 0) (\equiv D_{m m_E}^j)$ are the elements of the Wigner rotation matrix that connect the laboratory frame (with Z along \mathbf{E}) to the scattering frame (with z along \mathbf{k}). The Euler angles $(\phi_E, \theta_E, \chi_E)$ are the angles that define the direction of \mathbf{E} (where χ_E is taken as zero) in the scattering frame, $\hat{\mathbf{E}}$ (right panel of Supplementary Fig. 2).

The DCS for the $|jm_E \Omega \hat{\mathbf{E}}\rangle \rightarrow |j'm' \Omega' \epsilon'\rangle$ transition can be written as:

$$d\sigma(jm_E \Omega \hat{\mathbf{E}} \rightarrow j'm' \Omega' \epsilon') = \frac{1}{k^2} \left| F_{m'\epsilon' m_E \hat{\mathbf{E}}} \right|^2. \quad (8)$$

Summing over all final m' states

$$\begin{aligned} d\sigma(jm_E \Omega \hat{\mathbf{E}} \rightarrow j' \Omega' \epsilon') &= \frac{1}{k^2} \sum_{m'} \left| F_{m'\epsilon' m_E \hat{\mathbf{E}}} \right|^2 = \\ &= \frac{1}{2k^2} \sum_{m'} \left| \sum_m \sum_{\epsilon=e,f} \gamma_\epsilon D_{m m_E}^j F_{m'\epsilon' m \epsilon} \right|^2, \end{aligned} \quad (9)$$

where $\gamma_e = \alpha$ and $\gamma_f = \beta$. Note that in Eq. (9) m_E can have positive, $+|m_E|$, or negative, $-|m_E|$, values; when $m_E > 0$, $\alpha\beta = -|\alpha\beta|$ and when $m_E < 0$, $\alpha\beta = +|\alpha\beta|$. The DCS to a given final j' state is given by averaging over $m_E = \pm|m_E|$. After some algebra, it is possible to derive expressions with explicit dependence on the angles θ_E and ϕ_E that define the orientation of the electric field in the scattering frame. For $j = 1/2$, the result can be written as:

$$\left[d\sigma(j |m_E| \Omega \hat{E} \rightarrow j' \Omega' \epsilon') \right]_{\theta_E}^{\phi_E} = \frac{1}{2k^2} \left[\alpha^2 Q_1 - |\alpha\beta| \cos \theta_E Q_2 - |\alpha\beta| \sin \theta_E \cos \phi_E Q_3 + \beta^2 Q_4 \right], \quad (10)$$

where Q_1 – Q_4 are combinations of the various scattering amplitudes, $F_{m'\epsilon' \pm 1/2e}$. Specifically,

$$Q_1 = \sum_{m'} |F_{m'\epsilon' 1/2e}|^2 \quad (11)$$

$$Q_2 = \sum_{m'} (F_{m'\epsilon' 1/2f} F_{m'\epsilon' 1/2e}^* + c.c.) \quad (12)$$

$$Q_3 = \sum_{m'} (F_{m'\epsilon' -1/2f} F_{m'\epsilon' 1/2e}^* + c.c.) \quad (13)$$

$$Q_4 = \sum_{m'} |F_{m'\epsilon' 1/2f}|^2. \quad (14)$$

where *c.c.* stands for the complex conjugate of the previous term in the expression.

Eq. (10) can also be recast in terms of the *r*-PDDCSs [6],

$$\left[d\sigma(j |m_E| \Omega \hat{E} \rightarrow j' \Omega' \epsilon') \right]_{\theta_E}^{\phi_E} = \frac{\sigma_{\text{iso}}}{2\pi} \left\{ R_0^{(0)}(\theta) + 3\mathcal{A}_0^{(1)} [R_0^{(1)}(\theta) P_1(\cos \theta_E) + 2R_1^{(1)}(\theta) C_{11}(\theta_E, 0) \cos \phi_E] \right\}, \quad (15)$$

where σ_{iso} is the isotropic integral cross section in the presence of a field. $P_1(\cos \theta_E)$ is the first-order Legendre polynomial, and $C_{11}(\theta_E, 0) = -\frac{1}{\sqrt{2}} \sin \theta_E$ is the $k = 1$, $q = 1$ modified spherical harmonic, where $C_{kq}(\theta_E, \phi_E) = \left(\frac{4\pi}{2k+1} \right)^{1/2} Y_{kq}(\theta_E, \phi_E)$. The $\mathcal{A}_0^{(1)}$ coefficient is equal to $\langle P_1(\cos \theta_{\mu E}) \rangle$ which results in $-\frac{1}{3}|\alpha\beta|$. The crucial quantities in Eq. (15) are the *r*-PDDCSs, $R_q^{(k)}(\theta)$, which are the multipole moments of the expansion of the collision probability distribution of internuclear axes. It is evident from Eq. (15) that with a knowledge of the *r*-PDDCSs it is possible to determine the DCS resulting from any preparation of internuclear axis.

Comparison of Eqs. (10) and (15) leads to explicit expressions for the r -PDDCSs,

$$\frac{\sigma_{\text{iso}}}{2\pi} R_0^{(0)}(\theta) = \frac{1}{2k^2} (\alpha^2 Q_1 + \beta^2 Q_4) \quad (16)$$

$$\frac{\sigma_{\text{iso}}}{2\pi} R_0^{(1)}(\theta) = \frac{1}{2k^2} Q_2 \quad (17)$$

$$\frac{\sigma_{\text{iso}}}{2\pi} R_1^{(1)}(\theta) = -\frac{1}{2k^2\sqrt{2}} Q_3. \quad (18)$$

When the electric field is oriented along the scattering frame z -axis, $\theta_E = 0$ (corresponding to collisions taking place preferentially with the O-end of the molecule) or $\theta_E = \pi$ (for collisions preferentially oriented towards the N-end), the expression of the DCS is

$$\begin{aligned} \left[d\sigma(j | m_E | \Omega \hat{E} \rightarrow j' \Omega' \epsilon') \right]_{\theta_E=0 \text{ or } \pi} &= \frac{1}{2k^2} \left[\alpha^2 Q_1 \mp |\alpha\beta| Q_2 + \beta^2 Q_4 \right] \\ &= \frac{\sigma_{\text{iso}}}{2\pi} \left[R_0^{(0)}(\theta) \mp |\alpha\beta| R_0^{(1)}(\theta) \right]. \end{aligned} \quad (19)$$

Therefore, the z -orientation depends only on the $R_0^{(0)}(\theta)$ and $R_0^{(1)}(\theta)$ r -PDDCSs.

When the electric field is oriented along the scattering frame x -axis (as in the present experiment when scattering takes place in the plane of the molecular beams), $\theta_E = \pi/2$ and $\phi_E = 0$ or π . Consequently, Eqs. (10) and (15) reduce to

$$\begin{aligned} \left[d\sigma(j | m_E | \Omega \hat{E} \rightarrow j' \Omega' \epsilon') \right]_{\theta_E=\pi/2}^{\phi_E=0 \text{ or } \pi} &= \frac{1}{2k^2} \left[\alpha^2 Q_1 \mp |\alpha\beta| Q_3 + \beta^2 Q_4 \right] \\ &= \frac{\sigma_{\text{iso}}}{2\pi} \left[R_0^{(0)}(\theta) \pm \sqrt{2} |\alpha\beta| R_1^{(1)}(\theta) \right], \end{aligned} \quad (20)$$

with $\phi_E = 0$ ($+x$) or π ($-x$) for collisions preferentially oriented towards the N-side or the O-side, respectively. Thus, the only polarisation moments contributing to the DCS for side-on oriented collisions are the $R_0^{(0)}(\theta)$ and the $R_1^{(1)}(\theta)$ moments. These equations for the DCSs are also valid in the classical regime, where the QM $R_q^{(k)}(\theta)$ moments are replaced by their classical analogues [5, 6].

A further interesting case arises when the field is oriented with respect to the y -axis, that is, when the field is perpendicular to the scattering plane. In that case, $\theta_E = \pi/2$ and $\phi_E = \pi/2$ (or

$\phi_E = 3\pi/2$, Eqs. (10) and (15) become

$$\begin{aligned} \left[d\sigma(j | m_E | \Omega \hat{E} \rightarrow j' \Omega' \epsilon') \right]_{\theta_E=\pi/2}^{\phi_E=\pi/2 \text{ or } 3\pi/2} &= \frac{1}{2k^2} \left[\alpha^2 Q_1 + \beta^2 Q_4 \right] \\ &= \frac{\sigma_{\text{iso}}}{2\pi} R_0^{(0)}(\theta) = \frac{1}{2} \left[d\sigma_{+x}(\theta) + d\sigma_{-x}(\theta) \right]. \end{aligned} \quad (21)$$

The meaning of the $R_0^{(0)}(\theta)$ r -PDDCS is now clear: the DCS for the y -polarisation, when $j = 1/2$, is the sum of the separate contributions of the DCSs from the e and f states, resulting from the superposition of states under the electric field, weighted by the α^2 and β^2 coefficients. It therefore represents the actual isotropic DCS, resulting from the average of the DCSs for the $+x$ and $-x$ (or $+z$ and $-z$) orientations. However, it is important to note that the DCS for the y -axis polarisation, *i.e.* the isotropic DCS, is not the same as that which is obtained in the absence of an electric field. In the absence of a field, $\alpha = 0$ and $\beta = \sqrt{2}$ and the resulting DCS is

$$d\sigma(j \Omega f \rightarrow j' \Omega' \epsilon') = \frac{1}{k^2} Q_4 = \frac{1}{2k^2} \sum_{m,m'} |F_{m'\epsilon' m f}|^2, \quad (22)$$

exactly as what we would obtain for field-free scattering of a molecule initially selected in the Λ -doublet level.

The differential steric asymmetry for the x -orientation, defined as the difference between the calculated DCSs for the two orientations, $d\sigma_{+x}(\theta)$ and $d\sigma_{-x}(\theta)$, normalised by their sum, can be calculated directly from the r -PDDCSs,

$$d\sigma_{+x}(\theta) = d\sigma(\theta) \Big|_{\theta_E=\pi/2}^{\phi_E=0} = \frac{1}{k^2} \left[\alpha^2 Q_1 - |\alpha\beta| Q_3 + \beta^2 Q_4 \right] \quad (23)$$

$$d\sigma_{-x}(\theta) = d\sigma(\theta) \Big|_{\theta_E=\pi/2}^{\phi_E=\pi} = \frac{1}{k^2} \left[\alpha^2 Q_1 + |\alpha\beta| Q_3 + \beta^2 Q_4 \right]. \quad (24)$$

Hence,

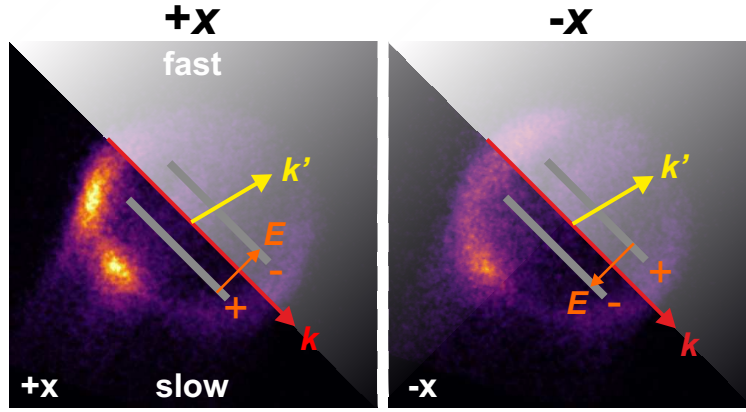
$$d\sigma_{\text{diff}}(\theta) = \frac{d\sigma_{+x}(\theta) - d\sigma_{-x}(\theta)}{d\sigma_{+x}(\theta) + d\sigma_{-x}(\theta)} = \frac{\sqrt{2} |\alpha\beta| R_1^{(1)}(\theta)}{R_0^{(0)}(\theta)}. \quad (25)$$

1.3 Data analysis

1.3.1 Experimental images

The experimentally measured scattering distributions obtained for the x -axis orientation are asymmetric around the initial relative velocity vector, \mathbf{k} , which makes the image analysis substantially more complicated than for images obtained in the z -axis (end-on) geometry, for which the distribution is symmetric around \mathbf{k} . Since in the scattering frame, the (positive) x -axis is defined by the direction of \mathbf{k}' , both the $+x$ and the $-x$ orientations are measured in a single experimental configuration. For this reason, in principle each ion image contains all the information required to determine the x -axis r -PDDCSs of interest. However, due to the different velocities of the molecules in the laboratory frame, the signal intensities are much stronger on the bottom left side of the images, where the laboratory velocity is slow and the detection probability therefore higher, than on the right side of the images, where the molecules move faster and therefore have a lower detection probability. For this reason, it is more reliable to determine the x -axis r -PDDCSs from sum and difference ion images recorded for different orientations of the static field, \mathbf{E} . Note that these differences in detection sensitivity for the fast and slow sides of the image lead to the asymmetry in the difference images shown in Fig. 2 of the main text, which would otherwise be exactly anti-symmetric around the relative velocity vector.

The difference in detection probability on the fast and slow side of the ion image must be taken into account when extracting information from the images, as will be described in Section 1.3.3 below. Because the signal is much stronger on the slow side, we will label the images according to the orientation that is detected on this side of the image. To illustrate this, the relative velocity vector, \mathbf{k} , the rods, and the electric field vector, \mathbf{E} , are superimposed on the experimental images for the $+x$ - (left) and the $-x$ -orientations (right) of the $\Delta j = 9$ transition in Supplementary Fig. 3. An example for the direction of the outgoing relative velocity vector, \mathbf{k}' , is shown in yellow, and correlates with the signal intensity on the slow side of the images. Note that the relative velocity after the collision is defined as $\mathbf{k}' = \mathbf{v}'_{\text{Ar}} - \mathbf{v}'_{\text{NO}}$, which means that the NO molecules move opposite to the direction of \mathbf{k}' .



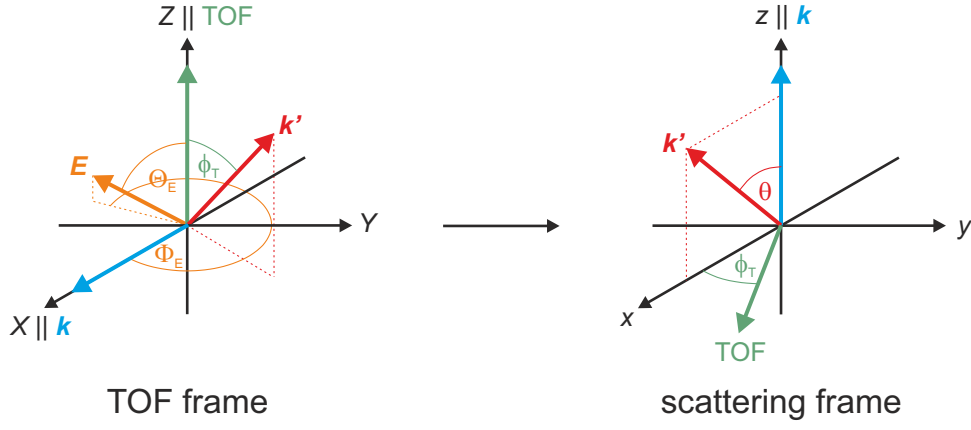
Supplementary Figure 3: Experimental images for $\Delta j = 9$ obtained in the $+x$ (left) and the $-x$ (right) geometries. The polarity of the rods and the resulting direction of the electric field are indicated; \mathbf{k} is represented by the red arrow, and an example direction for \mathbf{k}' is shown as a yellow arrow. Note that since $\mathbf{k}' = \mathbf{v}'_{\text{Ar}} - \mathbf{v}'_{\text{NO}}$, the NO molecules are moving in the direction opposite to \mathbf{k}' , corresponding with the signal on the slow side of the images.

In the image on the left, the electric field points in the same hemisphere as \mathbf{k}' (which corresponds with signal intensity on the slow side of the image), meaning that \mathbf{E} is along the positive x -axis in the scattering frame. In the image on the right, the electric field points opposite to the direction of \mathbf{k}' and thus points along the $-x$ -axis in the scattering frame.

1.3.2 Conversion from the time-of-flight frame to the scattering frame

In order to extract the differential cross sections (DCSs) from the experimental images, the parameters defined in the time-of-flight (TOF) frame (which should not be confused with the laboratory frame defined above) have to be rotated into the scattering frame. For our particular setup, the plane of the crossing molecular beams, which also contains the initial relative velocity vector, is perpendicular to the direction of the time-of-flight tube, which we take to be the Z -axis, as depicted in the left panel of Supplementary Fig. 4. In the scattering frame (right panel of Supplementary Fig. 4), which we have already defined above, the z -axis lies along \mathbf{k} . In addition, we define the azimuthal angle between the xz -plane and the TOF direction as ϕ_T . If \mathbf{k}' lies in the plane of the molecular beams, *i.e.* perpendicular to the TOF axis, then $\phi_T = \pi/2$. Following rotation matrix conventions of Zare [1], the angles of rotation for our system are $(\alpha, \beta, \gamma) = (\pi, -\pi/2, -\phi_T)$.

Let us start with the differential cross section for a specific pair of θ_E and ϕ_E angles (as given



Supplementary Figure 4: Relationship between the time-of-flight (TOF) frame and the scattering frame. The TOF axis and the relative velocity vectors before and after the collision, \mathbf{k} and \mathbf{k}' , are indicated in green, blue, and red, respectively. θ is the scattering angle and ϕ_T is the azimuthal angle of the TOF axis in the scattering frame. In the present experiments $\Theta_E = \pi/2$, $\Phi_E = \pi/2$ or $\Theta_E = \pi/2$, $\Phi_E = 3\pi/2$. Note also that for scattering of NO in the plane of the molecular beams (which is coincident with the ion image plane), $\phi_T = \pi/2$.

by Eq. (15) above). As a first step, the terms involving the scattering frame angles are expressed as modified spherical harmonic functions:

$$P_1(\cos \theta_E) = \cos \theta_E = C_{10}(\theta_E, \phi_E), \quad (26)$$

and

$$C_{11}(\theta_E, 0) \cos \phi_E = \frac{1}{2}[C_{11}(\theta_E, \phi_E) - C_{1-1}(\theta_E, \phi_E)]. \quad (27)$$

These modified spherical harmonics can now be rotated into the TOF frame using the Wigner rotation matrix with the Euler angles (α, β, γ) specified above:

$$C_{kq}(\theta_E, \phi_E) = \sum_{q'} D_{qq'}^k(\pi, -\frac{\pi}{2}, -\phi_T) C_{kq'}(\Theta_E, \Phi_E), \quad (28)$$

where the angles Θ_E and Φ_E describe the orientation of the electric field within the TOF frame (see left-hand side of Supplementary Fig. 4). Applying this transformation, it can be shown that

$$C_{10}(\theta_E, \phi_E) = \sin \Theta_E \cos \Phi_E, \quad (29)$$

and

$$C_{11}(\theta_E, 0) \cos \phi_E = -\frac{1}{\sqrt{2}}(\sin \phi_T \sin \Theta_E \sin \Phi_E + \cos \phi_T \cos \Theta_E). \quad (30)$$

Thus, the differential cross section can be rewritten in terms of the TOF frame coordinates:

$$\left[d\sigma(\theta) \right]_{\theta_E}^{\phi_E} = \frac{\sigma_{\text{iso}}}{2\pi} \left\{ R_0^{(0)}(\theta) + 3\mathcal{A}_0^{(1)} [R_0^{(1)}(\theta) \sin \Theta_E \cos \Phi_E - \sqrt{2}R_1^{(1)}(\theta)(\sin \phi_T \sin \Theta_E \sin \Phi_E + \cos \phi_T \cos \Theta_E)] \right\}. \quad (31)$$

For x -axis orientation, $\Theta_E = \pi/2$ and $\Phi_E = \pi/2$ or $3\pi/2$; consequently, the second term goes to zero, and the DCS simplifies to

$$\left[d\sigma(\theta) \right]_{\theta_E}^{\phi_E} = \frac{\sigma_{\text{iso}}}{2\pi} [R_0^{(0)}(\theta) - 3\sqrt{2}\mathcal{A}_0^{(1)}R_1^{(1)}(\theta)(\sin \phi_T \sin \Phi_E)]. \quad (32)$$

For the z -axis orientation the appropriate angles are $\Theta_E = \pi/2$, and $\Phi_E = 0$ or π .

1.3.3 Simulation and fitting of the experimental images

In order to determine the flux-density correction and thereby extract angular distributions from the ion images, the $+x$ and $-x$ experimental images were simulated using a Monte Carlo procedure, with the experimental parameters defining the space sampled during the simulation [10]. A polarisation correction, calculated from the apse model [10–12] (in which it was assumed that the collision induced rotational alignment for the $+x$ and $-x$ -orientations are the same), and the expression for the intrinsic scattering distribution, expressed in terms of the QM polarisation moments ($R_q^{(k)}(\theta)$), were used to model the intensity for a single ‘trajectory’, n , at a given detector position (x_n, y_n) [13]:

$$i(x_n, y_n, j, j', j^*, \chi_P) = z(x_n, y_n, j, j') P_{\text{scatt}}(\theta_n) A(x_n, y_n, j', j^*, \chi_P), \quad (33)$$

where $z(x_n, y_n, j, j')$ is an instrument function containing the flux-density correction, $P_{\text{scatt}}(\theta_n)$ is the intrinsic scattering probability, and $A(x_n, y_n, j', j^*, \chi_P)$ is the polarisation correction. The variables j and j' refer to the initial and final rotational state, j^* to the rotational level to which the NO is excited in the A state, and χ_P describes the polarisation of the excitation laser. The total intensity of an image is built from the sum of the individual trajectories in the Monte Carlo routine

(typically 10 million),

$$\begin{aligned}
I(x, y, j, j', j^*, \chi_P) &= \sum_n i(x_n, y_n, j, j', j^*, \chi_P) \\
&= \sum_n z(x_n, y_n, j, j') P_{\text{scatt}}(\theta_n) A(x_n, y_n, j', j^*, \chi_P),
\end{aligned} \tag{34}$$

and the total flux-density function is the sum of the flux-density corrections of all the trajectories, *i.e.*

$$Z(x, y, j, j') = \sum_n z(x_n, y_n, j, j'). \tag{35}$$

The images were fit to a set of modified spherical harmonic basis functions to calculate the experimental scattering probabilities and DCSs. Since for x -axis orientation the symmetry along the initial relative velocity vector, \mathbf{k} , is broken, it has proven more convenient to work with the experimental sum and difference images for the two orientations, from which the polarisation moments can be directly determined. In the case of the sum image, P_{scatt} is proportional to $R_0^{(0)}$, such that

$$I_{\text{sum}}(x, y, j, j', j^*, \chi_P) = \sum_n z(x_n, y_n, j, j') R_0^{(0)}(\theta_n) A(x_n, y_n, j', j^*, \chi_P). \tag{36}$$

For the difference image, we obtain

$$I_{\text{diff}}(x, y, j, j', j^*, \chi_P) = \sum_n z(x_n, y_n, j, j') [-6\sqrt{2} \mathcal{A}_0^{(1)} R_1^{(1)}(\theta_n) \sin \phi_{T_n}] \tag{37}$$

$$\times A(x_n, y_n, j', j^*, \chi_P). \tag{38}$$

Note that the intensity of the difference image is dependent on the angle ϕ_T , the azimuthal angle between \mathbf{k}' and the time-of-flight axis (see Supplementary Fig. 4). The polarisation moments appearing in the above expressions for the sum and difference images can be expanded as a series of modified spherical harmonics:

$$R_0^{(0)}(\theta) = \sum_n \frac{2n+1}{2} a_n C_{n0}(\theta, 0), \tag{39}$$

$$R_1^{(1)}(\theta) = \sum_n \frac{2n+1}{2} a_n C_{n1}(\theta, 0), \tag{40}$$

where the $C_{nm}(\dots)$ are the modified spherical harmonic functions of rank n and the a_n are the corresponding expansion coefficients. The intensity distributions of the sum and difference images can then be fit as a linear combination of basis functions containing the spherical harmonics,

$$I_{\text{sum/diff}}(x, y, j, j', j^*, \chi_P) = \sum_n \frac{2n+1}{2} a_n B_n(x, y, j, j', j^*, \chi_P), \quad (41)$$

with the basis functions for the sum and difference images given, respectively, by

$$B_n(x, y, j, j', j^*, \chi_P) = C_{n0}(\theta, 0) Z(x, y, j, j') A(x, y, j', j^*, \chi_P), \quad (42)$$

and

$$B_n(x, y, j, j', j^*, \chi_P) = -6\sqrt{2} \mathcal{A}_0^{(1)} C_{n1}(\theta, 0) \sin \phi_T Z(x, y, j, j') A(x, y, j', j^*, \chi_P). \quad (43)$$

These basis functions were generated by a Monte Carlo simulation and subsequently used to fit the experimental images in Fourier space with a genetic algorithm [10]. The resulting experimental polarisation moments, $R_0^{(0)}(\theta)$ and $R_1^{(1)}(\theta)$, were then substituted into Eq. (32) to determine the DCSs for the $+x$ - and $-x$ -orientation. The number of fitting modified spherical harmonic basis functions effectively determines the angular resolution of the experiments. Typically we use around 8 moments to fit the summed image, which corresponds to an angular resolution of around 20° .

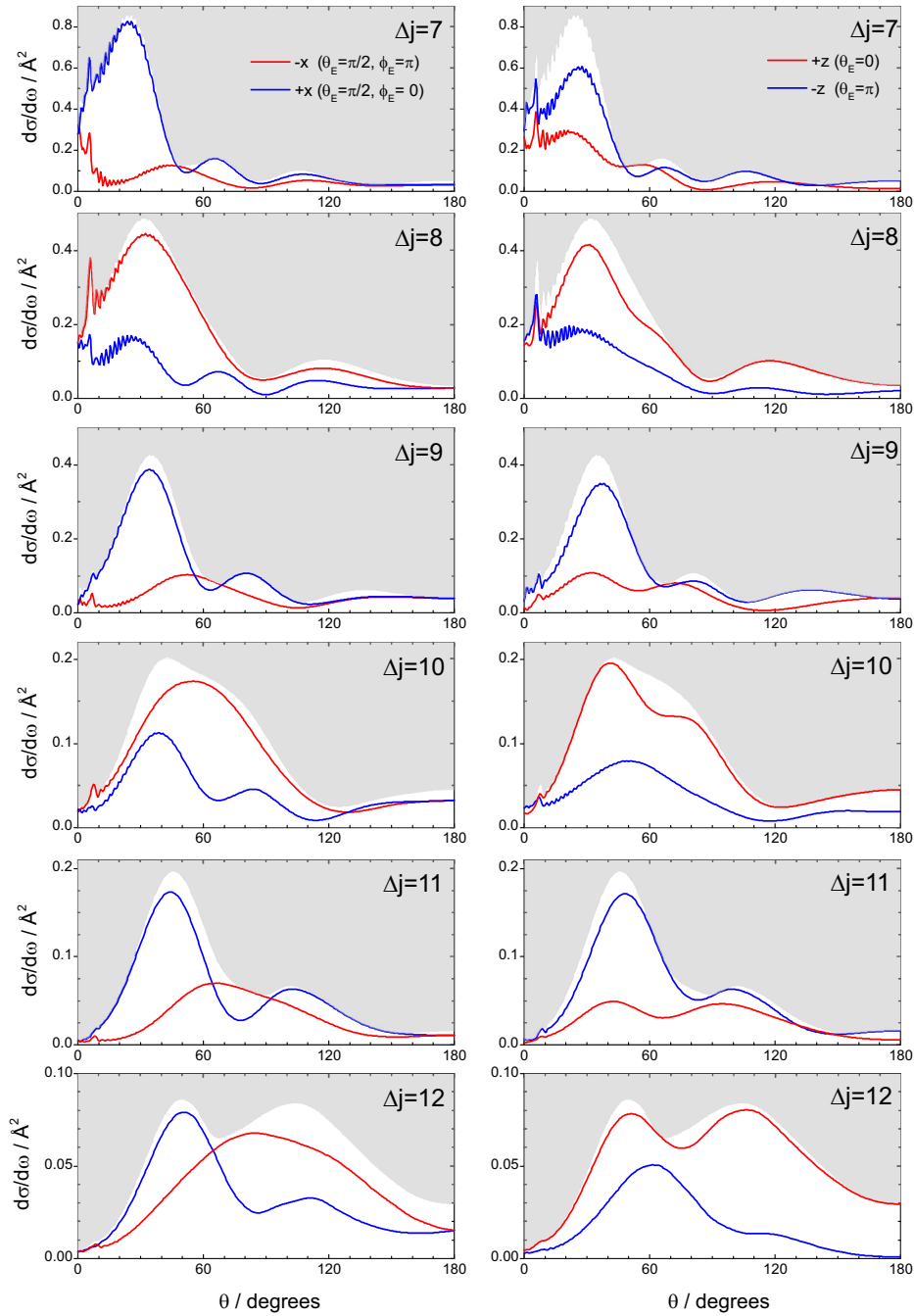
2 The origin of the structure in the x -axis oriented DCSs

In the following, we discuss the origin of the differences observed in the DCSs as a function of field direction that are described in the main text. In particular, we discuss in full the three factors mentioned in the main text which are primarily responsible for the form of the DCSs, namely the static field strength, the rotational rainbow structure, and quantum interference. We emphasise at the outset that the pattern of alternating DCS structures and intensities with field direction and Δj cannot be reproduced using classical trajectory methods, and is fundamentally quantum mechanical in nature.

2.1 DCSs for x - and z -axis orientation at infinite field

In the left panels of Supplementary Fig. 5 we show the effect of x -axis orientation on the QM DCSs for the same transitions as shown in Fig. 2 of the main text, but calculated in the limit of infinite field strength. Figure 3 of the main text shows a reduced data set for $\Delta j = 7$ and 12 only. Under these conditions, fully oriented $+\Omega$ or $-\Omega$ states can be selected, and the weights of the e and f Λ -doublets in the initial mixed state are equal. (In practice, such an infinite field would lead to mixing of different rotational states, as well as the Λ -doublets of excited rotational states, and the term *infinite field* is used here to indicate a field high enough to fully mix the Λ -doublet levels of the initial ground rotational state of NO(X), but not to mix the Λ -doublet levels of higher rotational states, or mix different rotational states, j .) Also displayed in the figure are the maximum possible DCSs obtained for any arbitrary orientation of the static field (bounded by the white areas). The clearest feature of these data is the alternation in intensities for $+x$ and $-x$ orientations depending on whether Δj is odd or even, respectively. Furthermore, for all Δj transitions, the DCSs obtained in the $+x$ orientation display more peaks than those for the $-x$ orientation, with the DCSs for the $+x$ orientation showing particularly pronounced forward scattering. The distinct scattering patterns for the $\pm x$ orientations correspond to different rotational rainbow structures, which can be rationalised in terms of constructively/destructively interfering ‘end-on’ and ‘side-on’ scattering paths at the two ends of the molecule, as described further below [3, 14, 15]. These, in turn, reflect the differences in the PESs and scattering dynamics for collisions towards the N- and O-ends of the molecule, with scattering towards the N-side occurring *via* more glancing (high impact parameter) collisions than that towards the O-side.

For comparison, the effect of the z -axis orientation (‘heads *versus* tails’ collisions) on the DCSs is shown in the right panels of Supplementary Fig. 5. Note that $+z$ refers to O-end collisions, whilst $-z$ refers to N-end collisions. Although the $+z$ - and $-z$ -configurations are clearly distinct, the differences in scattering pattern between the two ends are, in general, not as prominent as in the $\pm x$ -orientation, with the most forward scattered peak clearly present in both orientations. Furthermore, the $+x$ orientation for odd Δj and the $-x$ orientation for even Δj closely match the



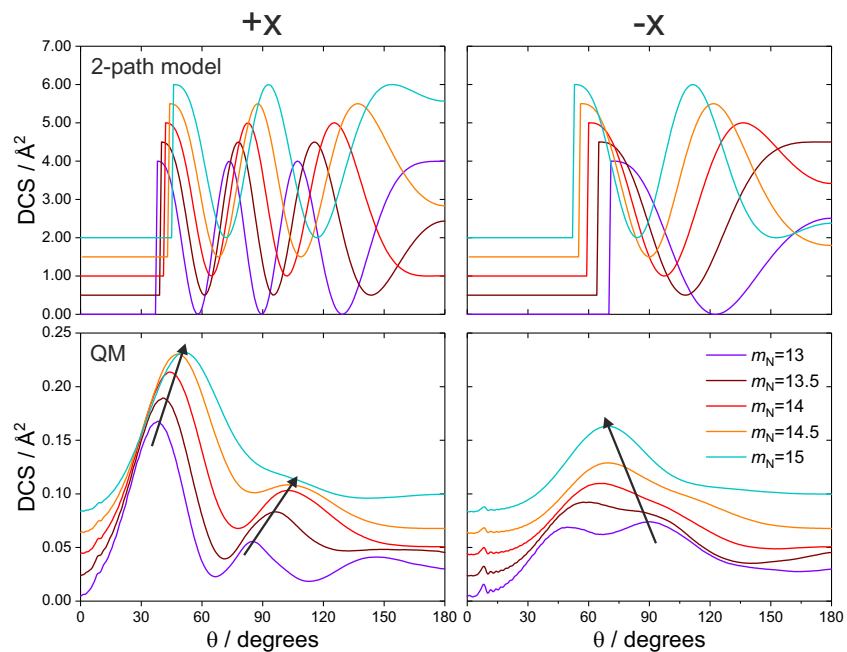
Supplementary Figure 5: QM x -axis (left panels) and z -axis (right panels) oriented DCSs for $\Delta j = 7$ to 12, as calculated in the limit of infinite static field strength. Orientations in which the Ar collides preferentially with the O-side/end of the molecule are represented in red ($-x$ and $+z$) while those that collide with the N-side/end are shown in blue ($+x$ and $-z$). The DCSs were maximised with respect to θ_E and ϕ_E and values above that maximum are shaded in grey. As is apparent from the figure, orientation along the x -axis is almost identical with the maximisation of the DCS in the forward hemisphere ($\theta < 90^\circ$).

maximum DCSs at forward and sideways scattering angles for low and medium Δj values (*e.g.*, for $\Delta j = 7$). Meanwhile, $\pm z$ -orientation dominates in the backward scattered region, especially for higher Δj transitions, where the DCS of the preferred orientation is very close to the maximised DCS (see, for example, the data for $\Delta j = 12$).

2.2 Orientation dependent rotational rainbow structure

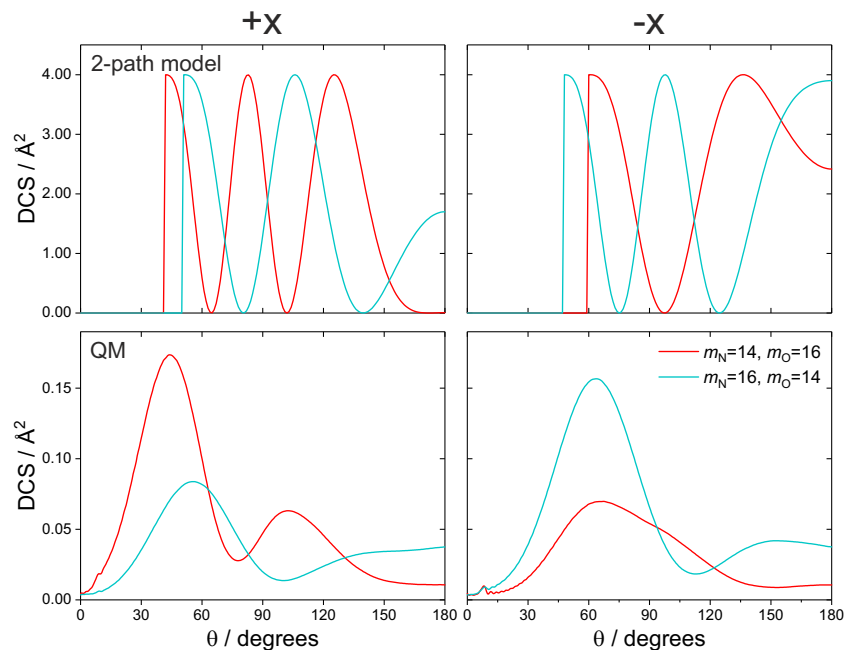
From a classical point of view, the comparatively smaller scattering angle of the strong forward peak in the $+x$ -orientation (repulsive collisions off the N-side) intuitively makes sense: if we consider the simple concept of a longer torque arm, or a larger range of impact parameters, on the N-side, we expect collisions towards the N-side to be more glancing, and thus more forward scattered, than collisions towards the O-side. To test the validity of this somewhat naive picture, we turn to a semi-classical 2-path model that describes the interference between trajectories at one end and one side of the NO molecule in terms of the phase difference between the two [14–16]. It should be emphasised that this simple 2-path model cannot be used to determine absolute cross sections, but does provide qualitative insight about the structure of the DCSs.

For the 2-path model calculations, the contour of the PES [17] at the experimental collision energy was used as a hard shell potential, and the phase difference between trajectories (or paths) impacting at one end and one side of the NO molecule was derived from the major and minor semi-axes of this ellipsoidal potential, as detailed in references [14–16, 18–20]. The resulting DCSs for $\Delta j = 11$ are shown in the top row of Supplementary Fig. 6 (red trace). It is immediately obvious that the interference between end-on and side-on trajectories at the N-side ($+x$) leads to more peaks in the DCS, and smaller scattering angles, than at the O-side ($-x$). Given that the centre of mass of the molecule is closer to the O-end, and that any attractive parts of the potential are ignored in the 2-path model, this is to be expected. We further expect the differences in scattering pattern for the two orientations to become more pronounced as the mass of the nitrogen is decreased, and more similar as the masses become more equal. To test this, we have performed the calculations with modified potential energy surfaces resulting from varying masses of the N and O atoms,



Supplementary Figure 6: DCSs for the $\Delta j = 11$ transition calculated with the 2-path model (top) and quantum mechanically on modified potentials (bottom). The QM data were obtained at infinite field strength. The data for the $+x$ and $-x$ orientations are shown on the left and right, respectively. Note that each trace is offset from the previous one by 0.5 (2-path model) and 0.02 (QM) units, respectively, in the order of increasing nitrogen mass. The nitrogen mass ranges from $N=13$ a.u. (purple) to $N=15$ a.u. (turquoise) in 0.5 a.u. steps. The arrows indicate the direction of the peak shift with increasing nitrogen mass. In all calculations, the mass of the oxygen was adjusted to keep the reduced mass of the NO constant.

consequently changing the value of the major semi-axis for either end of the molecule. The mass of the nitrogen atom was varied between 13 and 15 a.u. in 0.5 a.u. increments, and the mass of the O and the Ar atom was adjusted such that the reduced mass of the NO and the reduced mass of the NO + Ar system remained constant. The PES was re-expanded after each change in mass with the origin defined by the new centre of mass. The resulting DCSs for the modified mass combinations are shown in the top row of Supplementary Fig. 6. As the mass of the nitrogen is increased from 13 a.u. (purple line) to 15 a.u. (turquoise line), the peaks in the $+x$ orientation shift to larger scattering angles and have fewer maxima, while the peaks in the $-x$ orientation shift towards lower scattering angles and have more maxima. Effectively, as the centre of mass is shifted away from the nitrogen (and towards the oxygen) trajectories on the N-side have larger impact parameters and get deflected less. The opposite trend is observed in the $-x$ orientation,



Supplementary Figure 7: DCSs for the $\Delta j = 11$ transition calculated with the 2-path model (top) and quantum mechanically at infinite field strength (bottom). The data for the $+x$ and $-x$ orientations are shown on the left and right, respectively, with the original mass combination (N=14 a.u., O=16 a.u.) represented in red, and the combination in which the masses of the N and O are inverted (N=16 a.u., O=14 a.u.) represented in blue.

where the deflection becomes smaller as the centre of mass shifts away from the oxygen.

Although these observations are based on simple semi-classical ideas, a comparison with the full QM calculations on the modified potentials for the different mass combinations reveals similar trends, as shown in the bottom panels of Supplementary Fig. 6. Note that the QM calculations were run at infinite field strength for consistency with the data shown in Supplementary Fig. 5. As in the 2-path model, the peaks shift towards larger scattering angles and have fewer maxima in the $+x$ orientation as the nitrogen mass is increased, while the opposite trend is observed for the $-x$ orientation.

Figure 7 explores the effect of exchanging the masses of the nitrogen and the oxygen atoms on the DCS. In the 2-path model, the effect of inverting the masses of the N and O atoms (N=16 a.u., O=14 a.u., blue trace) results in lower scattering angles and more oscillations in the $-x$ -orientation than in the $+x$ -orientation, consistent with the trends observed in Supplementary Fig. 6. Quite strikingly, the QM DCS for the inverted mass combination in the $+x$ ($-x$)-orientation (shown in

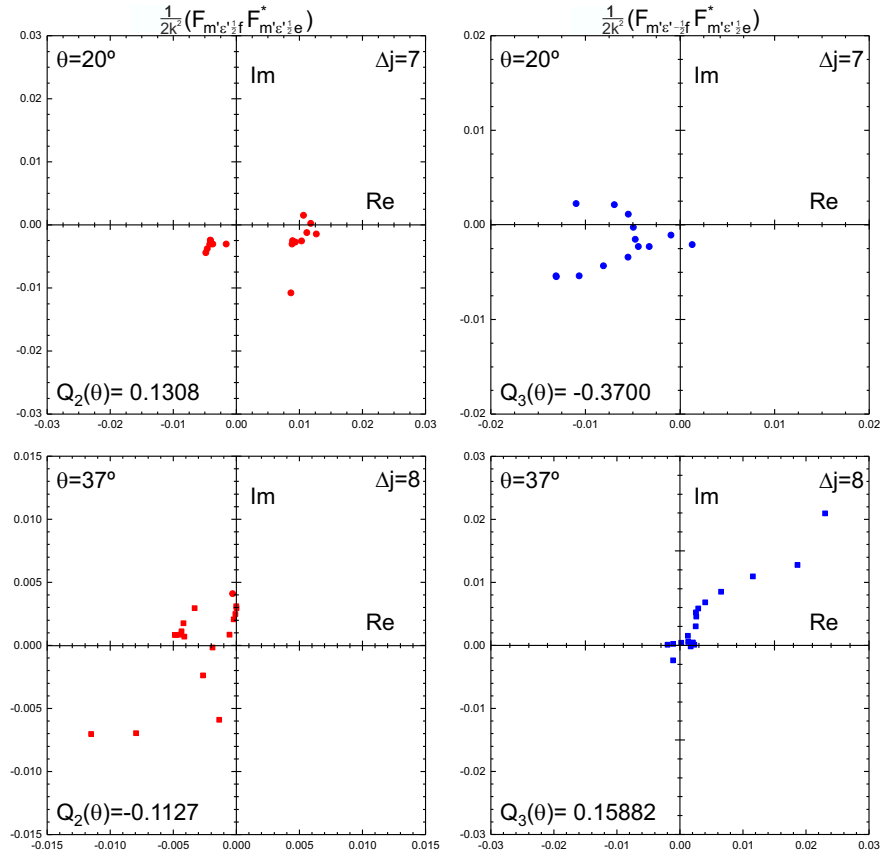
the bottom row of Supplementary Fig. 7) is very similar to the DCS for the natural mass combination (N=14 a.u., O=16 a.u., red trace) in the $-x$ ($+x$)-orientation. The fact that the DCSs in the two orientations are not exactly switched around when the masses are inverted indicates that the mass asymmetry and, to a lesser extent, the asymmetry of the PES, play a role in determining the observed differential steric effect. It is also noteworthy that the overall preference for the inverted mass combination is for the $-x$ -orientation, while for the natural masses, it is the $+x$ -orientation that dominates for $\Delta j = 11$. This provides direct evidence that the position and number of peaks originate from interfering “classical trajectories”, while the subtler differences between the two mass combinations are due to the differences in the potential at the two ends of the molecule.

From this analysis, we conclude that, in the $+x$ geometry (repulsive scattering off the N-side of NO), trajectories that are minimally deflected are favoured, and give rise to a prominent peak in the forwards direction. A similar mechanism may be attributed to collisions off the O-side/end, with the most forward-scattered peak located at larger scattering angles due to larger deflections at this end of the molecule. While the position and number of peaks can be rationalised with semi-classical arguments, quantum mechanics needs to be considered to rationalise the preference for one orientation or another, as well as the variation in peak intensity.

2.3 Quantum interference effect on intensities

QM interference between alternative scattering paths plays an essential role in both the x - and z -axis field-dependent effects [21]. From Supplementary Fig. 5, and Figs. 2 and 3 of the main text, this interference is most clearly manifest as an enhancement in intensity (or magnitude of the DCS) of the $+x$ -orientation over those for the $-x$ -orientation when Δj is odd, and *vice versa* when Δj is even. These differences in DCSs are clearly observed in the intensities of the raw images shown in Fig. 2 of the main text, and result in the forward scattered peak being particularly intense in the $+x$ -orientation for odd Δj . They also influence the overall appearance of the difference images shown in Fig. 2 of the main text.

The role of QM interference in determining the alternating pattern of peak intensities in the



Supplementary Figure 8: Representation of the phases of the individual m' terms in the sum over the first term in Q_2 , Eq. (12) (left, red data points), and the first term in Q_3 , Eq. (13) (right, blue data points) in the complex plane. The data corresponds to the values calculated at scattering angles of $\theta = 20^\circ$ and $\theta = 37^\circ$ in the case of $\Delta j = 7$ (top row, circles) and $\Delta j = 8$ (bottom row, squares), respectively. The specific scattering angles were chosen based on their pronounced steric preference. Note the differences in quadrant for the points associated with odd and even Δj .

oriented DCSs is demonstrated by considering further the terms Q_2 and Q_3 defined in Eqs. (12) and (13). Recall that these terms are respectively responsible for the z -axis and x -axis orientation behaviour. The QM interference leads to a change in sign of Q_2 and Q_3 with Δj . These terms arise directly from the coherent superposition of the initial e and f Λ -doublet levels prepared in the static orienting field. Let us illustrate the effect with the terms appearing in the orientation along the x -axis, Eq. (10), in the limit of an infinite field. Consider each of the relevant scattering amplitudes $F_{m'e'\pm 1/2e}(\theta)$, rewritten in a shorthand notation:

$$F_{m'e'-1/2f} = r_{m',f} e^{i\phi_{m',f}}$$

$$F_{m'e'+1/2e} = r_{m',e} e^{i\phi_{m',e}},$$

where $r_{m',f}$ and $r_{m',e}$ are the respective moduli of each of the scattering amplitudes, and $\phi_{m',f}$, $\phi_{m',e}$ the respective phases.

Apart from a constant, the x -axis oriented DCS at a given scattering angle can be written as

$$\sum_{m'} \left| r_{m',f} e^{i\phi_{m',f}} + r_{m',e} e^{i\phi_{m',e}} \right|^2 = \sum_{m'} \left[r_{m',f}^2 + 2 r_{m',f} r_{m',e} \cos(\Delta\phi_{m'}) + r_{m',e}^2 \right], \quad (44)$$

where $\Delta\phi_{m'}$ is the difference of phases between the scattering amplitudes pertaining to the two Λ -doublets. The first and third terms in Eq. (44) represent the contribution to the DCS from $f \rightarrow e'$ and $e \rightarrow e'$ transitions, respectively; that is, Q_4 and Q_1 , in that order. The middle term represents the interference between the corresponding e and f scattering amplitudes, which in this case is Q_3 . Depending on the value of $\Delta\phi_{m'}$ the interference will be constructive or destructive [16].

To illustrate the interference effect for each m' , Supplementary Fig. 8 shows the products in Eq. (44) corresponding to the various m' values in the complex plane. The products ($F_{m'e'1/2f} F_{m'e'1/2e}^*$) (those appearing in Q_2 , Eq. (12)) and ($F_{m'e'-1/2f} F_{m'e'1/2e}^*$) (those appearing in Q_3 , Eq. (13)) are shown in the left and right panels of Supplementary Fig. 8, respectively, for $\Delta j = 7$ (top) and $\Delta j = 8$ (bottom). The scattering angles, indicated in the figure, are chosen as typical examples for which there is a clear alternation in sign with Δj .

The figure clearly demonstrates that going from the odd to the even Δj there is a change in relative phase $e^{i(\Delta\phi_{m'})}$ for the two transitions which is responsible for the change in sign in Q_2 or Q_3 with Δj . This behaviour reflects the underlying contributions of even (homonuclear) and odd (heteronuclear) terms in the PES for the two transitions. As can be concluded from this analysis, the integral and differential steric asymmetry and, in particular, its alternation between even and odd Δj transitions, is a genuine quantum mechanical interference effect that cannot be accounted for by classical arguments.

2.4 Dependence on the static field

As the orientation field is reduced, the DCSs for both the $+x$ and $-x$ orientations evolve into those observed in the field free case, namely the DCSs for $f \rightarrow e$ Λ -doublet resolved transitions in the

present experiments. It has previously been established that the DCSs for the field free $f \rightarrow e$ transitions display a parity effect due to which more peaks are observed when Δj is odd (overall parity-conserving transitions) than when Δj is even (overall parity-changing transitions) [3,14,15]. At the experimental field strength, the initial f Λ -doublet contributes around 66% to the amplitude of the mixed state, and it is for this reason that the multiple peaks are seen most clearly only for the odd Δj transitions in the $+x$ orientation. If the final f Λ -doublets had been probed, the multiply peaked DCSs would then have been observed most clearly for even Δj transitions in the $+x$ orientation. This behaviour is confirmed by the QM scattering calculations, and is also supported qualitatively by preliminary experimental data on the f final Λ -doublet levels.

References

- [1] Zare, R. N. *Angular momentum: understanding spatial aspects in chemistry and physics* (Wiley-Interscience, 2013).
- [2] Brouard, M. & Vallance, C. (eds.) *Tutorials in Molecular Reaction Dynamics* (Royal Society of Chemistry, Cambridge, 2012).
- [3] Nichols, B. *et al.* Steric effects and quantum interference in the inelastic scattering of NO(X) + Ar. *Chem. Sci.* **6**, 2202–2210 (2015).
- [4] Alexander, M. H. Polarization and steric effects in inelastic collisions of NO($X^2\Pi$) with Ar and He. *Faraday Discuss.* **113**, 437–454 (1999).
- [5] Brouard, M. *et al.* Stereodynamics in NO(X) + Ar inelastic collisions. *J. Chem. Phys.* **144**, 224301 (2016).
- [6] Aoiz, F. J., Martínez, M. T. & Sáez-Rábanos, V. Quasi-classical treatment of the stereodynamics of chemical reactions: $\mathbf{k-r-k'}$ vector correlation for the Li + HF($v = 1, j = 1$) \rightarrow LiF + H reaction. *J. Chem. Phys.* **114**, 8880–8896 (2001).

- [7] Alexander, M. H. & Stolte, S. Investigation of steric effects in inelastic collisions of NO(X) with Ar. *J. Chem. Phys.* **112**, 8017–8026 (2000).
- [8] Van Leuken, J. J., Bulthuis, J., Stolte, S. & Snijders, J. G. Steric asymmetry in rotationally inelastic state-resolved NO + Ar collisions. *Chem. Phys. Lett.* **260**, 595–603 (1996).
- [9] de Lange, M. J. L. *et al.* Steric asymmetry in state-resolved NO–Ar collisions. *Chem. Phys. Lett.* **313**, 491–498 (1999).
- [10] Eyles, C. J. *et al.* Fully Λ -doublet resolved state-to-state differential cross-sections for the inelastic scattering of NO(X) with Ar. *Phys. Chem. Chem. Phys.* **14**, 5403–5419 (2012).
- [11] Khare, V., Kouri, D. J. & Hoffman, D. K. On j_z -preserving propensities in molecular collisions. I. Quantal coupled states and classical impulsive approximations. *J. Chem. Phys.* **74**, 2275–2286 (1981).
- [12] Hoffman, D. K., Evans, J. W. & Kouri, D. J. The kinematic apse and j_z -preserving propensities for nonreactive, dissociative, and reactive polyatomic collisions. *J. Chem. Phys.* **80**, 144–148 (1984).
- [13] Brouard, M. *et al.* Rotational alignment effects in NO (X)+ Ar inelastic collisions: An experimental study. *J. Chem. Phys.* **138**, 104310 (2013).
- [14] Eyles, C. J. *et al.* Interference structures in the differential cross-sections for inelastic scattering of NO by Ar. *Nat. Chem.* **3**, 597–602 (2011).
- [15] Eyles, C. J. *et al.* The effect of parity conservation on the spin-orbit conserving and spin-orbit changing differential cross sections for the inelastic scattering of NO(X) by Ar. *Phys. Chem. Chem. Phys.* **14**, 5420–5439 (2012).
- [16] McCurdy, C. W. & Miller, W. H. Interference effects in rotational state distributions: Propensity and inverse propensity. *J. Chem. Phys.* **67**, 463–468 (1977).

- [17] Alexander, M. H. A new, fully ab initio investigation of the NO($X^2\Pi$)–Ar system. I. Potential energy surfaces and inelastic scattering. *J. Chem. Phys.* **111**, 7426–7434 (1999).
- [18] Korsch, H. J. & Schinke, R. Rotational rainbows: An IOS study of rotational excitation of hard-shell molecules. *J. Chem. Phys.* **75**, 3850–3859 (1981).
- [19] Bosanac, S. Two-dimensional model of rotationally inelastic collisions. *Phys. Rev. A* **22**, 2617–2622 (1980).
- [20] Bosanac, S. & Buck, U. Rotational rainbow scattering from an off-center rigid shell model. *Chem. Phys. Lett.* **81**, 315 – 319 (1981).
- [21] Gijbbersen, A., Linnartz, H., Taatjes, C. A. & Stolte, S. Quantum interference as the source of steric asymmetry and parity propensity rules in NO-rare gas inelastic scattering. *J. Am. Chem. Soc.* **128**, 8777–8789 (2006).